Preprints of the 22nd IFAC World Congress
Yokohama, Japan, July 9-14, 2023

Nonlinear Model-Based Control of a Pneumatically Driven Robot

Kathrin Hoffmann * **Christian Trapp** **
Alexander Hildebrandt ** **Oliver Sawodny** *

* *Institute for System Dynamics, University of Stuttgart, D-70563 Stuttgart, Germany (e-mail: {kathrin.hoffmann, sawodny}@isys.uni-stuttgart.de).*
** *Robotics System Design, Festo SE & Co. KG, D-73734 Esslingen, Germany*

Abstract: In robotics, pneumatic drives are an interesting alternative to classic electric drives, as their physical properties enable the design of safe, lightweight and intuitively operable robots. In this work, a nonlinear model-based feedback control concept for a robot with 4 compressed-air-driven rotary joints is presented. The robot model comprising kinetics and pressure dynamics is formulated. For this drive type, significant nonlinear friction effects are present, which is known to be challenging for controller design, especially since there is no output-side measurement of the effective drive torque after subtracting friction. A control concept based on differential flatness, here with the particular case of feedback linearization, is derived, which is particularly well suited for a system with such effects. The algorithm contains both kinetics and pressure dynamics in one central controller, and its working principle and practical implications are discussed. With experimental results, the effectiveness of the trajectory tracking controller is demonstrated and insights into the components of this controller are provided.

Keywords: robotics, nonlinear control, tracking control, feedback linearization, flatness-based control, pneumatics

1. INTRODUCTION

Pneumatic actuators are widely used in automation because of their high power-to-weight ratio, durability, and cost-effectiveness. Due to their physical properties they are also attractive as flexible joints (De Luca and Book (2016)) in robots with multiple degrees of freedom (DOF). In contrast to most state-of-the-art electric robot drives, a particular feature of pneumatic drives is that they are direct drives without gears. This reduces the inertia, and, consequently, the kinetic energy in case of a collision, which increases safety. Moreover, they are inherently compliant because of the compressibility of air. A further consequence is that pneumatic manipulators are much lighter in weight.

As actuators for pneumatic robots, so far usually fluidic muscles (Tondu et al. (2005); Bou Saba et al. (2019)) and bellows for soft robots (Falkenhahn et al. (2017)) are employed. A design that is less common in the literature, but reduces model complexity and kinematic uncertainty are pneumatic robots with rigid links and flexible rotary joints. This facilitates the development of real-time feasible model-based controllers and has the potential to achieve higher precision. The robot must, first of all, be able to track trajectories, what in literature for pneumatic manipulators with coupled joints was reported with only medium accuracy (Bobrow and McDonell (1998); Mattiazzo et al. (2002); Taghia et al. (2012)). Thereafter, the control can be extended for collaborative applications, e.g. by force control. Meanwhile, the typical challenges of pneumatics persist: The low mechanical stiffness of the direct drive in combination with the compressibility of air makes the system prone to vibrations. Further there are nonlinearities in the pressure dynamics, air flow and valve characteristics, and for position control, which is the focus of this contribution, especially friction in the seals of the actuator. For the nonlinear dynamic friction, no exact model is available and, without an output-side joint torque sensor, the effective drive torque after subtracting the friction is not known.

In robot control, algorithms are usually split up into a trajectory tracking controller for the mechanics, and controllers for the actuators generating the torque, nested in one another. The outer loop robot controller is often based on feedback linearization, known as computed torque controller (Siciliano et al. (2009)). Also for the control of pneumatic actuators, researchers have found that nonlinear control laws based on input-output linearization perform better than linear ones (Brun et al. (1999)). Combining the above-mentioned inner and outer loop, for pneumatic manipulators this has led to the typical cascaded controller (Hildebrandt et al. (2003); Falkenhahn et al. (2017); Hoffmann et al. (2021)).

In contrast to that, we design in this work one central controller that comprises both kinetics and pressure dynamics, i.e., the actuator dynamics are included in the overall feedback linearizing controller. Such feedback-linearizing control (Isidori (1995)), which is a particular case of differential flatness approaches (Rothfuß (1997)), has been implemented for single pneumatic actuators (Hildebrandt

Fig. 1. Robot with pneumatic rotary joints (Festo SE & Co. KG (2018)).

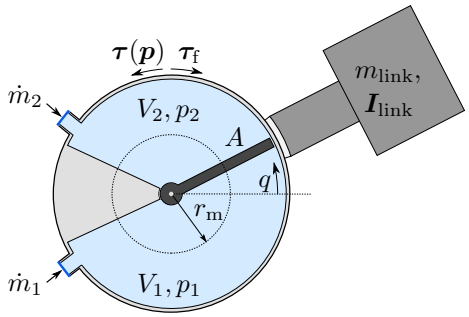

Fig. 2. Schematics of one pneumatic rotary joint.

et al. (2002); Aschemann and Hofer (2004)), for which the computational complexity is still low. The authors Bou Saba et al. (2019) applied flatness-based control to a system with three pneumatic muscle actuators. Their control law contains flatness-based feedforward, i.e., only an open-loop compensation of the nonlinearities, and a PI feedback controller. In contrast, what distinguishes our control algorithm is that the flatness-based component is based on feedback linearization, i.e., incorporated in the closed loop.

Our contribution is the trajectory tracking control of a robot with pneumatic rotary joints by this nonlinear controller accounting for the distinct properties of this drive type. It is one central controller, as opposed to the state-of-the-art cascaded robot controllers. The proposed structure has advantages in the presence of torque disturbances, as the friction here, that are elaborated in this paper. Although the control law for the present manipulator becomes much more complex than in the literature on single drives, we derive it systematically and implement it in a modular way. We show experimentally that the algorithm leads to a trajectory tracking accuracy, which is for pneumatic drives with their significant friction effects, very good.

This paper is structured as follows: The mechanical and pneumatic model of the robot is introduced in Section 2. Building upon this, the flatness-based feedback control law is derived in Section 3. Experimental results of the robot trajectory tracking controller are presented in Section 4, and the paper is concluded in Section 5.

2. ROBOT MODEL

The subject of this research is a robot as shown in Fig. 1, with pneumatically driven revolute joints schematically depicted in Fig. 2. Each of the four drives, indexed with i, consists of two pressure chambers separated by a swivel wing of area A_i and effective radius $r_{\mathrm{m},i}$, which is semi-rotatable to $\pm 135°$. A pressure difference between the chambers 1 and 2 of the actuator i generates the driving torque

$$\tau_i(p_{i,1}, p_{i,2}) = A_i r_{\mathrm{m},i}(p_{i,1} - p_{i,2}). \tag{1}$$

The pressure in each chamber is set individually by a mass flow $\dot{m}_{i,\{1,2\}}$ into or out of the chamber. This section states the dynamic model of the robot, including results from parameter identification.

The dynamic model of the robot mechanics reads

$$\boldsymbol{M}(\boldsymbol{q})\,\ddot{\boldsymbol{q}} + \boldsymbol{C}(\boldsymbol{q}, \dot{\boldsymbol{q}})\,\dot{\boldsymbol{q}} + \boldsymbol{G}(\boldsymbol{q}) = \boldsymbol{\tau}(\boldsymbol{p}) - \boldsymbol{\tau}_\mathrm{f} \tag{2}$$

where $\boldsymbol{q} \in \mathbb{R}^n$ with $n = 4$ is the vector of joint angles, $\boldsymbol{M}(\boldsymbol{q})$ is the inertia matrix, $\boldsymbol{C}(\boldsymbol{q}, \dot{\boldsymbol{q}})$ the Coriolis matrix, $\boldsymbol{G}(\boldsymbol{q})$ the vector of gravitational torques, $\boldsymbol{\tau}_\mathrm{f}$ the vector of friction torques, and $\boldsymbol{\tau}(\boldsymbol{p})$ the vector of driving torques (1). For the present 4 DOF robot, the model is derived with the Lagrange formalism using the geometric and dynamic parameters from CAD data.

A detailed overview of the pneumatic model can be found in Hoffmann et al. (2021). In the context of the present work, only the pressure differential equation needs to be considered. It reads

$$\dot{p}_{i,c} = \frac{\eta}{V_{i,c}(q_i)} \left(RT\dot{m}_{i,c} - \dot{V}_{i,c}(\dot{q}_i)\, p_{i,c} \right), \tag{3}$$

for each chamber $c \in \{1, 2\}$ of actuator i, and is controlled by the mass flow $\dot{m}_{i,c}$. In this equation, $V_{i,c}(q_i)$ is the chamber volume, η the polytropic index, R the specific gas constant, and T the temperature. Since the valves are installed next to the drive, the tubes are so short that the mass flow to and from the pressure chamber is assumed to be equal to the mass flow set by the valves.

As the pressure chambers and the rotatable swivel wing have to be sealed all around to avoid leakage, there is significant friction between these parts. With the use of a suitable lubricant, it is achieved that no Stribeck effect occurs. Friction is identified experimentally before installing the drive, while once built into the robot, no output-side torque measurement and thus no knowledge of the friction is available. Fig. 3 depicts the measured friction torque in joint 2 as a function of angular velocity and shows that hysteresis occurs. Such effects can be modeled by dynamic friction models from literature, such as Olsson et al. (1998); Pennestrì et al. (2016). However, a fit for the above measurement results in a very stiff ordinary differential equation, which can numerically only be solved with step sizes of less than 1 ms, and is therefore not real-time capable on the target system. To achieve the maximum possible frictional compensation in model-based controller design at a low complexity, a static fit of the form

$$\tau_{\mathrm{f},i} = f_{\mathrm{c},i} \tanh\left(\frac{\dot{q}_i}{\dot{q}_{\mathrm{c},i}} \right) + f_{\mathrm{v},i}\, \dot{q}_i \tag{4}$$

is approximated. It contains Coulomb friction with torque f_c and viscous friction with coefficient f_v of joint i, and a velocity threshold $\dot{q}_\mathrm{c}$ for transition effects at low velocities. For joint 2 (see Fig. 3), the Coulomb friction torque is 4.04 Nm, which is about 5 % of the maximum driving torque of 80 Nm. Joints 3 and 4 are of a smaller build, with maximum driving torque of 10 Nm and Coulomb friction torque of 1 Nm, so 10 % of the maximum driving

torque is needed to compensate for friction. To overcome these significant effects, a pressure difference of 0.56 bar is required.

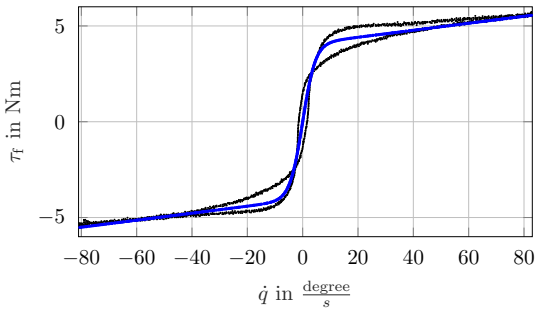

Fig. 3. Measured friction torque (black) and static fit (blue) with $f_\mathrm{c} = 4.04$ Nm and $f_\mathrm{v} = 0.0183\ \frac{\text{Nm s}}{\text{degree}}$ of joint 2.

3. CONTROLLER DESIGN

In the following, the mass flows

$$\boldsymbol{u} = [\dot{m}_{1,1}\ \dot{m}_{1,2}\ \dot{m}_{2,1}\ \cdots\ \dot{m}_{n,2}]^\intercal \in \mathbb{R}^{2n} \tag{5}$$

are taken as the control input to the system. Details on the subordinate mass flow controller acting on the valves can be found in Hoffmann et al. (2021).
Let $\boldsymbol{x} = [\boldsymbol{q}^\intercal\ \dot{\boldsymbol{q}}^\intercal\ \boldsymbol{p}^\intercal]^\intercal \in \mathbb{R}^{4n}$ with $\boldsymbol{p} = [p_{1,1}\ p_{1,2}\ p_{2,1}\ \dots\ p_{n,2}]^\intercal$ be the state vector. The variables $\boldsymbol{q}$ and $\boldsymbol{p}$ are available through measurement. The joint angular velocities $\dot{\boldsymbol{q}}$ are obtained by filtering and differentiation of $\boldsymbol{q}$. The overall mechanics and pressure dynamics constitute a nonlinear input affine multiple input multiple output (MIMO) system of the form

$$\dot{\boldsymbol{x}} = \boldsymbol{f}(\boldsymbol{x}) + \sum_{j=1}^{2n} \boldsymbol{g}_j(\boldsymbol{x})\, u_j, \quad \boldsymbol{x}(0) = \boldsymbol{x}_0. \tag{6}$$

The vector fields therein are

$$\boldsymbol{f} = \begin{bmatrix} \dot{\boldsymbol{q}} \\ \boldsymbol{M}^{-1}\left(-\boldsymbol{C}\dot{\boldsymbol{q}} - \boldsymbol{G} - \boldsymbol{\tau}_\mathrm{f} + \boldsymbol{\tau}(\boldsymbol{p})\right) \\ -\eta\ \mathrm{diag}\left(\frac{\dot{V}_{1,1}}{V_{1,1}}, \frac{\dot{V}_{1,2}}{V_{1,2}}, \frac{\dot{V}_{2,1}}{V_{2,1}}, \cdots, \frac{\dot{V}_{n,2}}{V_{n,2}}\right)\boldsymbol{p} \end{bmatrix} \tag{7}$$

$$\boldsymbol{g}_j = \begin{bmatrix} \boldsymbol{0}_{2n\times 1} \\ \frac{\eta RT}{V_j}\mathbf{e}_j \end{bmatrix}, \tag{8}$$

where $\mathbf{e}_j \in \mathbb{R}^{2n}$ is the j-th unit vector, and the arguments have been omitted for clarity.

The nonlinear MIMO system (6)–(8) is feedback linearizable by static feedback with respect to the outputs joint angle $\boldsymbol{z}_1 = \boldsymbol{q}$ and mean pressure $\boldsymbol{z}_2 = \boldsymbol{p}_\mathrm{m} = (\boldsymbol{p}_1 + \boldsymbol{p}_2)/2$. Consequently, the system is differentially flat with respect to this output $[\boldsymbol{z}_1,\ \boldsymbol{z}_2]^\intercal$, see Rothfuß (1997). The exact state linearizability can be easily verified by computing the Lie derivatives and checking the system's vector relative degree (Isidori (1995)). For the present robot, the components of the vector relative degree are $\rho_1 = 3$ for $\boldsymbol{z}_1$ and $\rho_2 = 1$ for $\boldsymbol{z}_2$. It is well-defined for all physically admissible $\boldsymbol{x}$, taking into account that $\boldsymbol{M}$ is positive definite, and that $V_{i,c} > 0$ because of a dead volume.

Differentiating the flat outputs according to their relative degree yields the equation for input-output coupling

$$\begin{bmatrix} \dddot{\boldsymbol{q}} \\ \dot{\boldsymbol{p}}_\mathrm{m} \end{bmatrix} = \underbrace{\begin{bmatrix} L_{\boldsymbol{f}}^3\boldsymbol{q} \\ L_{\boldsymbol{f}}\boldsymbol{p}_\mathrm{m} \end{bmatrix}}_{\boldsymbol{a}} + \underbrace{\begin{bmatrix} L_{\boldsymbol{g}_1}L_{\boldsymbol{f}}^2\boldsymbol{q} & \dots & L_{\boldsymbol{g}_{2n}}L_{\boldsymbol{f}}^2\boldsymbol{q} \\ L_{\boldsymbol{g}_1}\boldsymbol{p}_\mathrm{m} & \dots & L_{\boldsymbol{g}_{2n}}\boldsymbol{p}_\mathrm{m} \end{bmatrix}}_{\boldsymbol{\kappa}} \boldsymbol{u} \tag{9}$$

with $\boldsymbol{a} \in \mathbb{R}^{2n\times 1}$ and coupling matrix $\boldsymbol{\kappa} \in \mathbb{R}^{2n\times 2n}$. For physical interpretation, writing out the components of (9) as time derivatives instead of Lie derivatives yields

$$\boldsymbol{a} = \begin{bmatrix} \frac{\mathrm{d}}{\mathrm{d}t}(\boldsymbol{M}^{-1})\boldsymbol{M}\ddot{\boldsymbol{q}} + \boldsymbol{M}^{-1}\left(-\dot{\boldsymbol{C}}\dot{\boldsymbol{q}} - \boldsymbol{C}\ddot{\boldsymbol{q}} - \dot{\boldsymbol{G}} - \dot{\boldsymbol{\tau}}_\mathrm{f} + \dot{\boldsymbol{\tau}}_{p,\dot{V}}\right) \\ \dot{\boldsymbol{p}}_{\mathrm{m},\dot{V}} \end{bmatrix}. \tag{10}$$

Therein, the vector $\dot{\boldsymbol{\tau}}_{p,\dot{V}}$ with components

$$\dot{\tau}_{p,\dot{V},i} = -A_i r_{\mathrm{m},i}\eta\left(\frac{p_{i,1}\dot{V}_{i,1}}{V_{i,1}} - \frac{p_{i,2}\dot{V}_{i,2}}{V_{i,2}}\right) \tag{11}$$

is the change of the driving torque $\boldsymbol{\tau}(\boldsymbol{p})$ due to compression or expansion of the chamber, and $\dot{\boldsymbol{p}}_{\mathrm{m},\dot{V}}$ with components

$$\dot{p}_{\mathrm{m},\dot{V},i} = -\frac{\eta}{2}\left(\frac{p_{i,1}\dot{V}_{i,1}}{V_{i,1}} + \frac{p_{i,2}\dot{V}_{i,2}}{V_{i,2}}\right) \tag{12}$$

is the change of the mean pressure $\boldsymbol{p}_\mathrm{m}$ for the same reason. The coupling matrix reads

$$\boldsymbol{\kappa} = \begin{bmatrix} \eta RT\,\boldsymbol{M}^{-1}\boldsymbol{\Lambda}_1 \\ \frac{\eta RT}{2}\boldsymbol{\Lambda}_2 \end{bmatrix} \tag{13}$$

with block diagonal matrices for the joint geometry

$$\boldsymbol{\Lambda}_1 = \mathrm{diag}\left(A_1 r_{\mathrm{m},1}\begin{bmatrix}\frac{1}{V_{1,1}} & \frac{-1}{V_{1,2}}\end{bmatrix}, \cdots, A_n r_{\mathrm{m},n}\begin{bmatrix}\frac{1}{V_{n,1}} & \frac{-1}{V_{n,2}}\end{bmatrix}\right) \tag{14a}$$

$$\boldsymbol{\Lambda}_2 = \mathrm{diag}\left(\begin{bmatrix}\frac{1}{V_{1,1}} & \frac{1}{V_{1,2}}\end{bmatrix}, \cdots, \begin{bmatrix}\frac{1}{V_{n,1}} & \frac{1}{V_{n,2}}\end{bmatrix}\right) \tag{14b}$$

and has full rank for all physically admissible robot configurations. Using the above terms, the control law

$$\boldsymbol{u}(\boldsymbol{x}) = \boldsymbol{\kappa}^{-1}(\boldsymbol{x})\ \left(\boldsymbol{\nu} - \boldsymbol{a}(\boldsymbol{x})\right). \tag{15}$$

describes a static input transformation that effects an input-output linearization and decoupling. This renders the nonlinear system (6)–(8) a system of decoupled integrator chains with new input $\boldsymbol{\nu}$, known as Brunovsky canonical form (Isidori (1995)). In this canonical form, the state vector becomes $\boldsymbol{z} = [\boldsymbol{z}_1,\ \dot{\boldsymbol{z}}_1,\ \ddot{\boldsymbol{z}}_1,\ \boldsymbol{z}_2]^\intercal$.

To track reference trajectories $\boldsymbol{z}^*$, a linear controller

$$\boldsymbol{\nu} = \underbrace{\begin{bmatrix} \dddot{\boldsymbol{z}}_1^* \\ \dot{\boldsymbol{z}}_2^* \end{bmatrix}}_{\boldsymbol{\nu}_\mathrm{FF}} + \underbrace{\begin{bmatrix} \boldsymbol{K}_2(\ddot{\boldsymbol{z}}_1^* - \ddot{\boldsymbol{z}}_1) + \boldsymbol{K}_1(\dot{\boldsymbol{z}}_1^* - \dot{\boldsymbol{z}}_1) + \boldsymbol{K}_0(\boldsymbol{z}_1^* - \boldsymbol{z}_1) \\ \boldsymbol{K}_{\boldsymbol{p}_\mathrm{m}}(\boldsymbol{z}_2^* - \boldsymbol{z}_2) \end{bmatrix}}_{\boldsymbol{\nu}_\mathrm{FB}} \tag{16}$$

is designed, containing feedforward $\boldsymbol{\nu}_\mathrm{FF}$ and stabilizing feedback $\boldsymbol{\nu}_\mathrm{FB}$. Its feedback gains $\boldsymbol{K}_{\{.\}}$ are chosen as diagonal matrices. The resulting dynamics of the tracking errors $e_{1,i} = z_{1,i}^* - z_{1,i}$ for joint angle q_i, and $e_{2,i} = z_{2,i}^* - z_{2,i}$ for mean pressure $p_{\mathrm{m},i}$ in the closed loop are for each joint i

$$\dddot{e}_{1,i} + K_{2,ii}\ddot{e}_{1,i} + K_{1,ii}\dot{e}_{1,i} + K_{0,ii}e_{1,i} = 0 \tag{17a}$$

$$\dot{e}_{2,i} + K_{p_\mathrm{m},ii}e_{2,i} = 0. \tag{17b}$$

The error dynamics of each joint are decoupled from those of the other joints, according to the Brunovsky normal form, and become asymptotically stable by a suitable choice of feedback gains. The block diagram of the overall control structure is shown in Fig. 4. In the present work, feedback linearization is carried out, i.e., (10) and (13) are computed using measured signals. Only the friction term

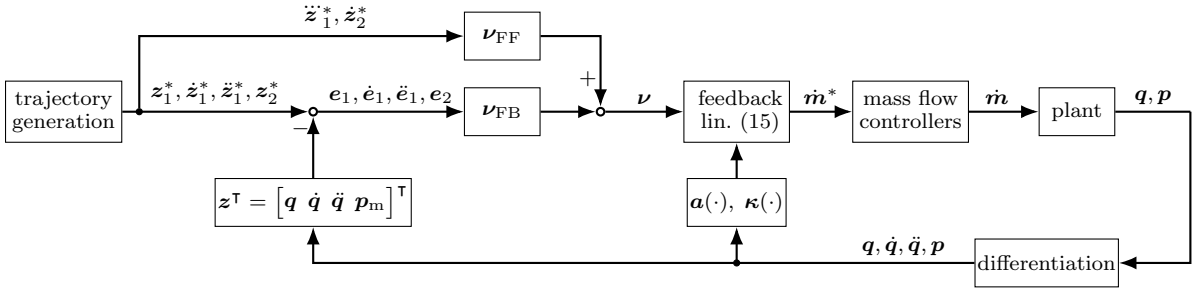

Fig. 4. Block diagram of the control structure.

$$\dot{\tau}_{\mathrm{f}}{}^* = \frac{\partial \tau_{\mathrm{f}}^*}{\partial \dot{q}^*} \ddot{q}^* \tag{18}$$

in (10) is implemented as feedforward with desired quantities (superscript *), which reduces noise, and, at the same time, intervenes earlier to set the joint in motion.

While state-of-the-art computed torque trajectory tracking controllers in robotics are implemented in the torque / acceleration domain, the present flatness-based controller acts in the jerk domain and has a direct feedthrough to the pressure dynamics. This control on a differential level entails some structural differences. For the friction compensation, it implies that no frictional torque, but its derivative is applied as feedforward control. The corresponding term (18) contains the derivative of the static friction model (4) with respect to $\dot{q}$, as depicted in Fig. 5. At the start of a joint motion, this peak is multiplied with a desired acceleration in the direction of motion. In the control law (15), this results in an aeration mass flow peak in one chamber and a deaeration mass flow peak in the other, increasing the pressure difference in the actuator. This increases the drive torque, enabling the joint to break loose from stiction. To brake the joint, the above peak is multiplied with a desired acceleration against the direction of motion, leading to mass flow peaks in the opposite direction, reducing the driving torque. In experiments, this second part of friction during deceleration was omitted, and a better position accuracy was achieved without this term. This is because pure feedforward compensation of friction can be inexact, first, in the presence of tracking errors $e, \dot{e}, \ddot{e}$, and second, due to friction model inaccuracies. The remaining, not feedforward controlled, friction effects must be compensated by feedback. The feedback in the controller in this work also has structural differences compared to classic torque domain controllers. These differences are explained in the next section.

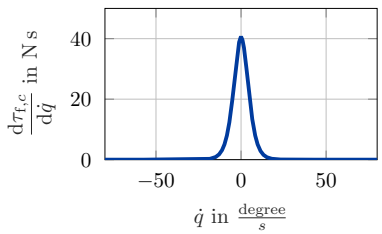

Fig. 5. Derivative of static friction model with respect to angular velocity, as required for friction feedforward. Parameter values of joint 2.

4. EXPERIMENTAL RESULTS AND DISCUSSION

For the experiments, the algorithm is tested on the 4 DOF robot, using a dSPACE rapid prototyping system running at 1 kHz. The feedback controller gains for the flat output $z_1 = q$ are chosen by pole placement, which results for the four joints in bandwidths {0.8, 1.1, 3.0, 3.7} Hz. With this tuning, good trajectory tracking is possible, while the gains are low enough to avoid valve chattering. The supply pressure is 7 bar absolute, and the desired mean pressure p_{m}^* is chosen to be 3.5 bar constant, allowing a wide range of pressure differences to drive the actuator. The feedback controller for the flat output $z_2 = p_{\mathrm{m}}$ is tuned with a bandwidth of 10 Hz for all joints.

In the measurements shown in the following, the robot tracks a C^3 trajectory in joint coordinates, which covers the typical workspace. Fig. 6 depicts the desired and actual joint angles and corresponding errors. The largest tracking errors occur at the beginning of joint motions when friction is not exactly compensated. Especially for joints 1 and 2, which are strongly coupled via the off-diagonal elements of the mass matrix, the control law decouples the two axes, so that no significant errors from coupling effects occur. At the end of joint motions, the tracking errors decrease, and all joints achieve steady-state errors below 0.3°. This is where the flatness-based controller shows its structural advantage. Although no integral part is contained in (16), the controller has inherently integrating behavior with respect to the joint angle. The reason is that the tracking error leads in (15) to a control mass flow, which enters the pressure in integral form, increasing the pressure difference, and thus driving torque. This drives the joint towards its desired angle. This effect can be seen for example around $t = 30$ s, especially for joint 2, where a continuous decrease of the tracking error occurs. The restriction is that the proportional gain of (16) should not be too large to avoid friction-induced limit cycles around the target position. Note that the feedback is implemented in the coordinates $z = [q\ \dot{q}\ \ddot{q}\ p_{\mathrm{m}}] \in \mathbb{R}^{4n}$. From a theoretical point of view (Isidori (1995)), these are obtained by a state transformation $z(x)$, where $\ddot{q} = \ddot{z}_1 = L_f^2 q = M^{-1}(-C\dot{q} - G - \tau_{\mathrm{f}} + \tau(p))$, i.e., a model-based acceleration reconstruction. In the present controller, however, the measured instead of the calculated acceleration is used in the feedback (16), because the coordinate transformation has in practice the disadvantage that it contains model errors, while the measured signal is free of them. For visualization, consider the case in which position and/or velocity errors are present so that feedback thereof effects an additional torque to reduce this error. Such extra torque would cause an additional acceleration in the model, which in practice may not occur in the presence of unmodeled friction effects. This erroneous $\ddot{q}$ would then counteract the other components in the feedback and limit the controller performance. In the experiment, this results in larger

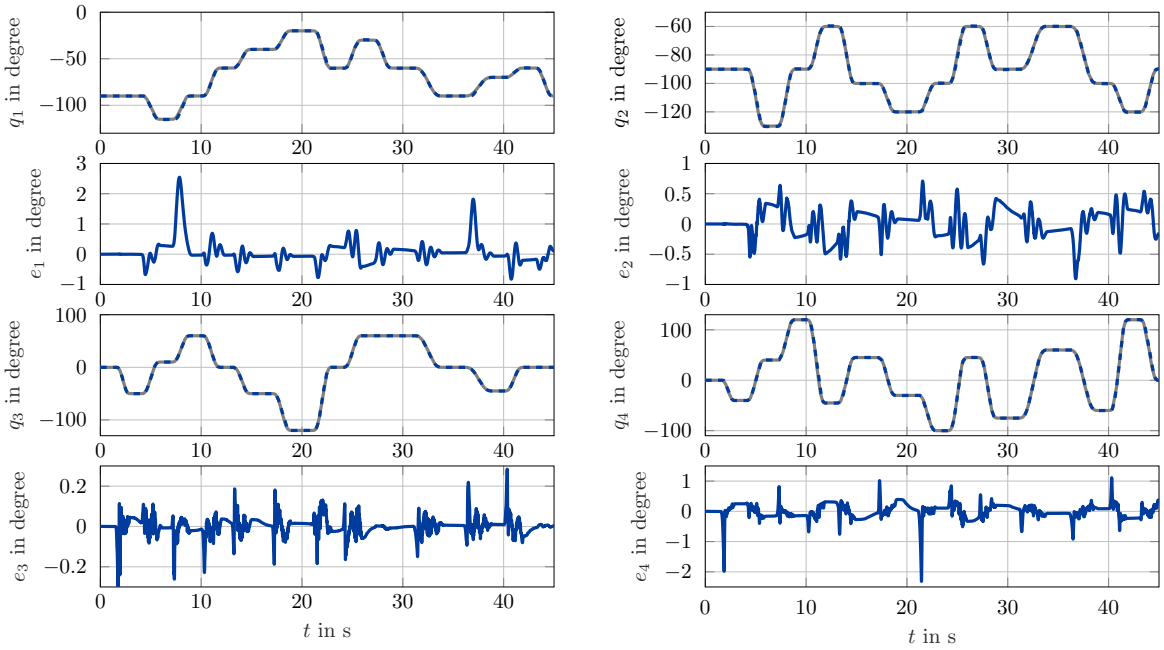

Fig. 6. Desired (—) and actual (- - -) joint angle, and corresponding tracking error of all joints.

stationary errors, and only with the measured instead of calculated $\ddot{\boldsymbol{q}}$ the previously described integrating behavior is achieved.

The angular acceleration signal cannot be directly measured, as in the current prototype no acceleration sensors are installed. Instead, the angular acceleration signal is obtained by filtering and differentiation of the angle measurements. This is feasible with the present high-resolution encoders, but is noisy, which is a well-known problem in the literature (Belanger et al. (1998)). Alternatively, the acceleration can be estimated with an observer, which, however, increases the influence of the model uncertainties, especially due to friction.

The previously described acceleration feedback also distinguishes the present central controller from state-of-the-art cascaded control of pneumatics, where the joint angle controller is implemented in the torque domain with only position and velocity feedback. The feedback of the measured acceleration in this control structure is on the same differential level as not measurable friction torque disturbances so that the latter are directly included in the feedback. This is particularly advantageous at the beginning of joint motions, where an acceleration error due to friction occurs first, before velocity and position errors result.

To summarize, this central controller contains other mechanisms to compensate for friction than state-of-the-art cascaded control of pneumatic manipulators. Since pneumatic drives are characterized by nonlinear, dynamic friction effects that vary over time, in friction feedforward control there occur torque errors, especially at velocities close to zero. These errors must be compensated by feedback, for which the feedback path in the present controller is well suited.

For the above robot motion, some details about the composition of the control signal are given next, exemplary for joint 2. Fig. 7 shows the components of the compensation term (10). It is noticeable that the largest nonlinearity to be compensated by the controller comes from the pressure differential equation $\boldsymbol{M}^{-1}\dot{\boldsymbol{\tau}}_{p,\dot{V}}$. Also clearly recognizable is the peak at the beginning of each joint motion, originating from the derivative of Coulomb friction. The gravity component plays a role, too. Smaller, in contrast, is the term with the time derivative of the inverse mass matrix, and even smaller the Coriolis terms, so that the latter are omitted from the figure. For a robot with multiple DOF, the terms in the top part of (10) require a computational effort beyond that of computed torque controllers. In our current experiments, executing the algorithm on the rapid prototyping system is real-time feasible. For target hardware with less computing power, however, it is advisable to neglect comparatively small terms, which are typically $\frac{\mathrm{d}}{\mathrm{d}t}(\boldsymbol{M}^{-1})\boldsymbol{M}\ddot{\boldsymbol{q}}$, $\boldsymbol{M}^{-1}\dot{\boldsymbol{C}}\dot{\boldsymbol{q}}$ and $\boldsymbol{M}^{-1}\boldsymbol{C}\ddot{\boldsymbol{q}}$, depending on the robot mechanics.

Fig. 8 shows the components of the controller (15). The nonlinearity compensation term $\boldsymbol{\kappa}^{-1}(-\boldsymbol{a})$ is clearly visible, especially in the middle of transitions. As for the feedback in the linearized system, the position feedback $\boldsymbol{\kappa}^{-1}\left[\, \boldsymbol{K}_0(\boldsymbol{z}_1^* - \boldsymbol{z}_1),\ \boldsymbol{0}_{n\times 1}\,\right]^\intercal$ and the velocity feedback $\boldsymbol{\kappa}^{-1}\left[\, \boldsymbol{K}_1(\dot{\boldsymbol{z}}_1^* - \dot{\boldsymbol{z}}_1),\ \boldsymbol{0}_{n\times 1}\,\right]^\intercal$ are smaller than the nonlinearity compensation term, which indicates good decoupling and linearization through the control law. The mean pressure feedback $\boldsymbol{\kappa}^{-1}\left[\, \boldsymbol{0}_{n\times 1},\ \boldsymbol{K}_{\mathrm{p_m}}(\boldsymbol{z}_2^* - \boldsymbol{z}_2)\,\right]^\intercal$ is much smaller than the other components, thus not depicted here, and the desired mean pressure is tracked well. At the beginning of most transitions, both $\boldsymbol{\kappa}^{-1}(-\boldsymbol{a})$ and the feedback $\boldsymbol{\kappa}^{-1}\boldsymbol{\nu}$ act in the same direction to follow the desired trajectory, while friction is under-compensated in $\boldsymbol{a}$, as common in practice. Especially from the middle of transitions onwards, the feedback is overlaid by noise, in particular from the measured acceleration signal. Specifically, the acceleration gain of the controller should not be chosen too large in order to keep the feedback of measurement noise into the system small. Despite this effect, the best compromise between trajectory tracking accuracy and noise was achieved with the present tuning parameters obtained by pole placement.

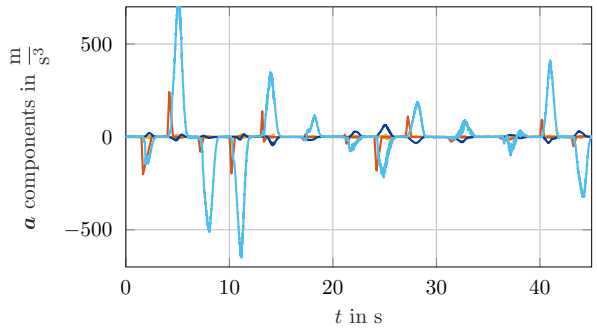

Fig. 7. Components of the compensation term $\boldsymbol{a}$, see (10), for joint 2: $\frac{\mathrm{d}}{\mathrm{d}t}(\boldsymbol{M}^{-1})\boldsymbol{M}\ddot{\boldsymbol{q}}$ (—), $\boldsymbol{M}^{-1}\dot{\boldsymbol{\tau}}_{\mathrm{f}}$ (—), $\boldsymbol{M}^{-1}\dot{\boldsymbol{G}}$ (—), $\boldsymbol{M}^{-1}\dot{\boldsymbol{\tau}}_{p,\dot{V}}$ (—).

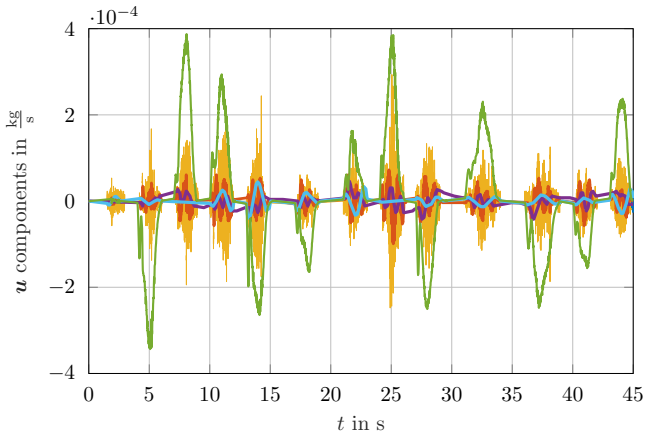

Fig. 8. Mass flow components of the control law (15): Acceleration feedback $\boldsymbol{\kappa}^{-1}\left[\, \boldsymbol{K}_2(\ddot{\boldsymbol{z}}_1^* - \ddot{\boldsymbol{z}}_1),\ \boldsymbol{0}_{n\times 1}\,\right]^\intercal$ (—), velocity feedback $\boldsymbol{\kappa}^{-1}\left[\, \boldsymbol{K}_1(\dot{\boldsymbol{z}}_1^* - \dot{\boldsymbol{z}}_1),\ \boldsymbol{0}_{n\times 1}\,\right]^\intercal$ (—), position feedback $\boldsymbol{\kappa}^{-1}\left[\, \boldsymbol{K}_0(\boldsymbol{z}_1^* - \boldsymbol{z}_1),\ \boldsymbol{0}_{n\times 1}\,\right]^\intercal$ (—), jerk feedforward $\boldsymbol{\kappa}^{-1}\left[\, \dddot{\boldsymbol{z}}_1^*,\ \boldsymbol{0}_{n\times 1}\,\right]^\intercal$ (—), and feedback linearization $\boldsymbol{\kappa}^{-1}(-\boldsymbol{a})$ (—).

5. CONCLUSION

In this paper, a model-based controller using the method of feedback linearization for a 4 DOF robot prototype with pneumatic rotary joints was presented. As a foundation, the mechanical and pneumatic models of the robot were given, and the measured dynamic friction effects were shown. With the system being feedback linearizable, the corresponding controller was derived. All nonlinearities are compensated based on measured signals, only frictional compensation is fed forward. For the exactly linearized system, decoupled controllers for angles and mean pressures of each joint are designed. Unlike state-of-the-art cascaded control of pneumatics, in the present central controller, a tracking error leads to a control mass flow, acting on the derivative of the pressure, i.e., the controller has integrating behavior with respect to the driving torque. Also, acceleration, which is on the same differential level as the disturbance torque, is included in the feedback, so that disturbance torques are handled well. For these reasons, the controller overcomes the significant nonlinear friction effects in the joints that can neither be fully controlled by model-based feedforward nor measured. Experimental trajectory tracking results demonstrate the effectiveness of the overall control concept. Additional insights into the components of the controller as well as the practical implications of this structure were discussed. Possible future work includes other approaches for acceleration reconstruction, such as model-based observers or additional acceleration sensors, to reduce the noise in this signal, which is fed back into the control loop.

REFERENCES

Aschemann, H. and Hofer, E.P. (2004). Flatness-based trajectory control of a pneumatically driven carriage with model uncertainties. *IFAC Proceedings Volumes*, 37(13), 225–230.

Belanger, P.R., Dobrovolny, P., Helmy, A., and Zhang, X. (1998). Estimation of angular velocity and acceleration from shaft-encoder measurements. *The International Journal of Robotics Research*, 17(11), 1225–1233.

Bobrow, J.E. and McDonell, B.W. (1998). Modeling, identification, and control of a pneumatically actuated, force controllable robot. *IEEE Transactions on Robotics and Automation*, 14(5), 732–742.

Bou Saba, D., Massioni, P., Bideaux, E., and Brun, X. (2019). Flatness-based control of a two degrees-of-freedom platform with pneumatic artificial muscles. *Journal of Dynamic Systems, Measurement, and Control*, 141(2).

Brun, X., Belgharbi, M., Sesmat, S., Thomasset, D., and Scavarda, S. (1999). Control of an electropneumatic actuator: Comparison between some linear and non-linear control laws. *Proceedings of the Institution of Mechanical Engineers, Part I: Journal of Systems and Control Engineering*, 213(5), 387–406.

De Luca, A. and Book, W.J. (2016). Robots with flexible elements. In *Springer Handbook of Robotics*, 243–282. Springer.

Falkenhahn, V., Hildebrandt, A., Neumann, R., and Sawodny, O. (2017). Dynamic control of the Bionic Handling Assistant. *IEEE/ASME Transactions on Mechatronics*, 22(1), 6–17.

Festo SE & Co. KG (2018). Collaborative robotics in production of the future.

Hildebrandt, A., Sawodny, O., Neumann, R., and Hartmann, A. (2002). A flatness based design for tracking control of pneumatic muscle actuators. In *7th International Conference on Control, Automation, Robotics and Vision*, 1156–1161.

Hildebrandt, A., Sawodny, O., Neumann, R., and Hartmann, A. (2003). A cascaded tracking control concept for pneumatic muscle actuators. In *European Control Conference (ECC)*, 2517–2522.

Hoffmann, K., Müller, D., Simon, R., and Sawodny, O. (2021). On trajectory tracking control of fluid-driven actuators. *at - Automatisierungstechnik*, 69(11), 970–980.

Isidori, A. (1995). *Nonlinear control systems*. Communications and control engineering series. Springer, London, 3. ed. edition.

Mattiazzo, G., Mauro, S., Raparelli, T., and Velardocchia, M. (2002). Control of a six-axis pneumatic robot. *Journal of Robotic Systems*, 19(8), 363–378.

Olsson, H., Åström, K.J., Canudas de Wit, C., Gäfvert, M., and Lischinsky, P. (1998). Friction models and friction compensation. *European Journal of Control*, 4(3), 176–195.

Pennestrì, E., Rossi, V., Salvini, P., and Valentini, P.P. (2016). Review and comparison of dry friction force models. *Nonlinear Dynamics*, 83(4), 1785–1801.

Rothfuß, R. (1997). *Anwendung der flachheitsbasierten Analyse und Regelung nichtlinearer Mehrgrößensysteme*. VDI-Verl., Düsseldorf.

Siciliano, B., Sciavicco, L., Villani, L., and Oriolo, G. (2009). *Robotics: Modelling, Planning and Control*. Springer, London.

Taghia, J., Wilkening, A., and Ivlev, O. (2012). Position control of soft-robots with rotary-type pneumatic actuators. In *7th German Conference on Robotics*.

Tondu, B., Ippolito, S., Guiochet, J., and Daidie, A. (2005). A seven-degrees-of-freedom robot-arm driven by pneumatic artificial muscles for humanoid robots. *The International Journal of Robotics Research*, 24(4), 257–274.